

Passive Synthetic Aperture Radar Imaging using Low-Rank Matrix Recovery Methods

Eric Mason, Il-Young Son and Birsen Yazıcı*, *Senior Member, IEEE*

Abstract—We present a novel image formation method for passive synthetic aperture radar (SAR) imaging. The method is an alternative to widely used Time Difference of Arrival (TDOA) or correlation-based backprojection method. These methods work under the assumption that the scene is composed of a single or a few widely separated point targets. The new method overcomes this limitation and can reconstruct heterogeneous scenes with extended targets.

We assume that the scene of interest is illuminated by a stationary transmitter of opportunity with known illumination direction, but unknown location. We consider two airborne receivers and correlate the fast-time bistatic measurements at each slow-time. This correlation process maps the tensor product of the scene reflectivity with itself to the correlated measurements. Since this tensor product is a rank-one positive semi-definite operator, the image formation lends itself to low-rank matrix recovery techniques. Taking into account additive noise in bistatic measurements, we formulate the estimation of the rank-one operator as a convex optimization with rank constrain. We present a gradient-descent based iterative reconstruction algorithm and analyze its computational complexity. Extensive numerical simulations show that the new method is superior to correlation-based backprojection in reconstructing extended and distributed targets with better geometric fidelity, sharper edges and better noise suppression.

Index Terms—Passive imaging, passive radar, passive synthetic aperture radar, low-rank matrix recovery.

I. INTRODUCTION

A. Motivation

In recent years, the growing availability of radio frequency sources of opportunity, such as radio, television and cell phone transmission stations, have lead to an increasing interest in passive radar applications [1]–[4], [4]–[8]. Removing the need to have a dedicated transmitter, passive radar systems offer many advantages such as stealth, simplicity and lowered cost.

Time or Frequency Difference of Arrival (TDOA/FDOA) or correlation-based backprojection is a widely used passive imaging and detection method [5], [6], [9]–[20]. These methods correlate two or more measurements obtained at different locations and matched filters the result based on time or frequency difference of arrival. TDOA is used to locate a

target/emitter and FDOA is used to estimate the radial velocity of a moving target. Although this approach is computationally efficient and straightforward to implement, it has major drawbacks: (1) It works under the assumption that the medium contains a single point target. This assumption can be relaxed in a statistical setting to include a few widely separated point targets [9], [11]–[13]. However, for two or more relatively close targets, this method produces spurious peaks that are called ghost targets. (2) TDOA/FDOA cannot detect/image densely distributed multiple point targets or extended targets. In this paper, we develop an alternative to TDOA based passive imaging based on low-rank matrix recovery. The new method overcomes the limitations of the TDOA or correlation-based approach and exhibits superior performance in reconstructing realistic SAR targets.

B. Related Work

Another widely used approach in passive imaging is based on bistatic time-of-flight measurements [21]–[29]. This approach requires knowledge of transmitter locations and transmitted waveforms and “reference receivers” with a direct line-of-sight to transmitters of opportunity. Within this framework, a variety of passive SAR imaging applications have been studied [30]–[37]. In [33] experimental results are presented using Envisat-1 satellite as an illuminator of opportunity, imagery is formed using a method based on CLEAN processing [27]. To improve resolution, the use of the TerraSAR-X satellite as an illuminator of opportunity is studied in [30]. Sources of opportunity that are relatively wideband, such as DVB-T and WiMAX, are of particular interest in passive radar. An analysis of DVB-T signal structure and different processing schemes have been studied in [8], [38]–[40]. WiMAX signals and associated image reconstruction methods have been studied in [1], [41], [42]. Doppler based backprojection methods using ultra-narrowband waveforms of opportunity have been studied in [15], [43]–[45].

Low-rank matrix recovery (LRMR) is the theory of rank minimization, analogous to compressive sensing [46], [47]. LRMR offers superior performance and theoretical guarantees in solving an inverse problem in which the rank of the matrix of interest is low [48], [49]. The LRMR theory is closely related to the theory matrix completion [50], [51]. The LRMR techniques have previously been applied to imaging problems in [52]–[56]. In [57] a convex LRMR method was presented to reconstruct images using correlated or interferometric measurements. In [52], [53] LRMR techniques have been applied to intensity-only imaging. In [54] an imaging problem in

Yazıcı is with the Department of Electrical, Computer and Systems Engineering, Rensselaer Polytechnic Institute, 110 8th Street, Troy, NY 12180 USA E-mail: B. Y. yazici@ecse.rpi.edu, Phone: (518)-276 2905, Fax: (518)-276 6261.

This work was supported by the Air Force Office of Scientific Research (AFOSR) under the agreement FA9550-12-1-0415, and by the National Science Foundation (NSF) under the Grant No. CCF-1218805.

*Corresponding author.

Copyright (c) 2014 IEEE. Personal use of this material is permitted. However, permission to use this material for any other purposes must be obtained from the IEEE by sending a request to pubs-permissions@ieee.org

which the number of antennas is larger than the number of targets resulting in a low rank model have been considered; and matrix completion methods have been used to decrease the number of required measurements. More generally, [55], [56] have presented a theory pertaining to the robustness of using interferometric measurements and the required number of measurements within convex optimization framework.

LRMR methods have been used as preprocessing techniques in SAR imaging. In [58] matrix completion has been used to estimate missing slow-time samples and the approach was shown to be superior to compressive sensing in improving the cross-range resolution. Similarly, in [59] LRMR was paired with robust principle component analysis to improve SAR cross-range resolution by interpolating the raw SAR data.

C. Overview and Advantages of Our Work

In this paper, we present a novel alternative to TDOA based backprojection imaging for passive SAR. We consider a stationary transmitter with known illumination direction, but unknown location and two airborne receivers deployed on the same or different platforms. We correlate fast-time measurements obtained at different slow-times. This correlation results in a linear forward model that maps a positive semi-definite rank one operator to correlated measurements. The positive semi-definite rank one structure of the operator results from taking the Kronecker product of the scene reflectivity with itself. We call this Kronecker product, the *Kronecker scene* and pose the image reconstruction as a rank minimization problem within a constrained convex optimization framework. Taking into account additive noise, we extend the rank-minimization based image formation to a statistical setting. We use a splitting method and address the resulting convex optimization problems using a projected gradient descent procedure with an acceleration [60]–[62]. We determine the scene reflectivity from the eigenvector of the estimated Kronecker scene corresponding to its maximum eigenvector.

The TDOA based backprojection relies on the assumption that the scene to be recovered is a collection of small number of point targets. It implicitly assumes that the scene reflectivity corresponds to the diagonal elements of the Kronecker scene. For this assumption to hold, all but one of the diagonal elements of the Kronecker scene must be zero. In such a case, the SAR scene must be composed of a point target. The new method allows us to recover extended targets and image a wider variety of realistic scenes.

Extensive numerical simulations verify the superiority of the new method over TDOA in reconstructing extended and dense distributed targets with better geometric fidelity, background noise suppression and robustness with respect to additive noise and phase errors. Furthermore, under the far-field and small scene assumptions, the new method does not require the knowledge of transmitter locations and transmitted waveforms.

While we specifically consider passive SAR imaging of stationary scenes, the method can be extended to include passive imaging of moving scenes, Doppler based imaging and passive multi-static imaging using stationary antennas [6], [11]–[13], [19], [43].

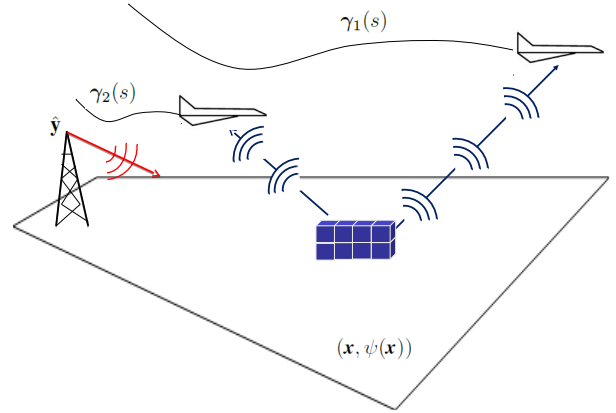


Fig. 1. A typical imaging scenario consisting of two receivers $\gamma_1(s)$ and $\gamma_2(s)$ flying arbitrary trajectories. The transmitter is stationary and illuminating the scene of interest.

D. Organization of the Paper

The rest of the paper is organized as follows: in Section II, we develop the forward model. In Section III, we present our image reconstruction method and algorithm for the noiseless and noisy measurements. In Section IV, we analyse the computational complexity of the algorithm. In Section V, we present numerical simulations to demonstrate its performance. Section VI concludes our paper.

II. MODEL FOR CORRELATED MEASUREMENTS

We assume that there are two airborne receivers flying over a scene of interest. These receivers may either be deployed on the same platform or on different platforms. A typical imaging geometry is depicted in Figure (1). Let $\gamma_i(s) \in \mathbb{R}^3, i = 1, 2, s \in S := [s_a, s_b]$ be the flight trajectory of i -th receiver, where s represents the slow-time.¹ Let ω be the frequency variable corresponding to fast-time. Let $\mathbf{x} = (\mathbf{x}, \psi(\mathbf{x})) \in \mathbb{R}^3$ denote the surface of the earth, where $\mathbf{x} = (x_1, x_2)$ and $\psi : \mathbb{R}^2 \rightarrow \mathbb{R}$ is a known ground topography. Let $\tilde{\rho} : \mathbb{R}^2 \rightarrow \mathbb{R}$ be the ground reflectivity.

A. Received Signal Model

We assume that the electromagnetic waves are propagating in free-space. Under the start-stop and Born approximations, the fast-time temporal Fourier transform of the received signal at the i -th receiver due to a transmitter located at \mathbf{y} , can be modelled as [9], [63]

$$f_i(\omega, s) \approx \mathcal{L}_i[\tilde{\rho}](\omega, s) := \int e^{i2\pi\omega r_i(s, \mathbf{x}, \mathbf{y})/c_0} \times A_i(\omega, s, \mathbf{x}, \mathbf{y}) \tilde{\rho}(\mathbf{x}) d\mathbf{x}, \quad i = 1, 2 \quad (1)$$

where

$$r_i(s, \mathbf{x}, \mathbf{y}) = |\mathbf{y} - \mathbf{x}| + |\mathbf{x} - \gamma_i(s)|, \quad (2)$$

¹In the context of passive radar imaging, slow-time, s , corresponds to the data processing window. Fast-time corresponds to the time scale within one data processing window.

$$A_i(\omega, s, \mathbf{x}) = \frac{\omega^2 J_{R_i}(\omega, s, \mathbf{x}) J_T(\omega, s, \mathbf{x})}{(4\pi)^2 |\boldsymbol{\gamma}_i(s) - \mathbf{x}| |\mathbf{x} - \mathbf{y}|}. \quad (3)$$

In (3), J_{R_i} and J_T represent the receiver and transmitter antenna beam patterns, which are the Fourier transform of the effective current density on the antennas and can include arbitrary waveforms. Additionally, this term contains the geometric spreading factors representing a loss in energy resulting from electromagnetic wave propagation. We assume that A_i is a slowly varying function of ω as described in [63] and that the signal is bandlimited such that $\omega \in \Omega := [\omega_a, \omega_b]$.

B. Forward model

For each slow-time s , we correlate the received signals in fast-time and obtain the following:

$$d_{ij}(\omega, s) = f_i(\omega, s) f_j^*(\omega, s), \quad i, j = 1, 2 \quad i \neq j \quad (4)$$

where f^* denotes the complex conjugate of f . Substituting (1) into (4), we obtain

$$d_{ij}(\omega, s) = \int e^{i2\pi \frac{\omega}{c_0} r_{ij}(s, \mathbf{x}, \mathbf{x}', \mathbf{y})} A_i(\omega, s, \mathbf{x}, \mathbf{y}) A_j^*(\omega, s, \mathbf{x}', \mathbf{y}) \times \tilde{\rho}(\mathbf{x}) \tilde{\rho}^*(\mathbf{x}') d\mathbf{x} d\mathbf{x}', \quad i, j = 1, 2 \quad i \neq j \quad (5)$$

where $r_{ij}(s, \mathbf{x}, \mathbf{x}', \mathbf{y}) = r_i(s, \mathbf{x}, \mathbf{y}) - r_j(s, \mathbf{x}', \mathbf{y})$, is the difference of the bistatic ranges from each receiver. Using the small-scene and far-field assumptions, we approximate the transmitter-to-scene distance using a Taylor series expansion around the points $\mathbf{x}, \mathbf{x}' = 0$,

$$\begin{aligned} |\mathbf{y} - \mathbf{x}| &\approx |\mathbf{y}| + \hat{\mathbf{y}} \cdot \mathbf{x} \\ |\mathbf{y} - \mathbf{x}'| &\approx |\mathbf{y}| + \hat{\mathbf{y}} \cdot \mathbf{x}', \end{aligned} \quad (6)$$

where $\hat{\mathbf{y}}$ denotes the unit vector in the direction of \mathbf{y} , i.e., the direction in which the transmitter is illuminating. Then, r_{ij} can be expressed as follows:

$$r_{ij}(s, \mathbf{x}, \mathbf{x}', \hat{\mathbf{y}}) = |\mathbf{x} - \boldsymbol{\gamma}_i(s)| - |\mathbf{x}' - \boldsymbol{\gamma}_j(s)| + \hat{\mathbf{y}} \cdot (\mathbf{x} - \mathbf{x}'). \quad (7)$$

Note that under the small-scene and far-field assumptions, the range difference r_{ij} no longer depends on the transmitter locations.

We define

$$\mathcal{R} := \tilde{\rho} \otimes \tilde{\rho}^* \quad (8)$$

where \otimes denotes the Kronecker or tensor product. Thus, \mathcal{R} is a rank-one, positive semi-definite operator with kernel

$$\rho(\mathbf{x}, \mathbf{x}') = \tilde{\rho}(\mathbf{x}) \times \tilde{\rho}^*(\mathbf{x}'). \quad (9)$$

We refer to ρ as the *Kronecker scene*. (9) shows that the unknown scene reflectivity $\tilde{\rho}$ is contained within the rank-one, positive semi-definite operator \mathcal{R} whose kernel is ρ . In fact, $\tilde{\rho}$ is the eigenvector of \mathcal{R} .² Using the phase term (7) and (8), (9), we approximate (5) as follows:

$$\begin{aligned} d_{ij}(\omega, s) &\approx \mathcal{F}_{ij}[\mathcal{R}](\omega, s) \\ &:= \int e^{i2\pi \omega r_{ij}(s, \mathbf{x}, \mathbf{x}', \hat{\mathbf{y}})/c_0} A_{ij}(\omega, s, \mathbf{x}, \mathbf{x}', \mathbf{y}) \times \rho(\mathbf{x}, \mathbf{x}') d\mathbf{x} d\mathbf{x}' \quad i, j = 1, 2 \quad i \neq j \end{aligned} \quad (10)$$

²Note that (9) is also known as outer-product of two vectors in signal processing.

where

$$r_{ij}(s, \mathbf{x}, \mathbf{x}', \hat{\mathbf{y}}) = |\mathbf{x} - \boldsymbol{\gamma}_i(s)| - |\mathbf{x}' - \boldsymbol{\gamma}_j(s)| + \hat{\mathbf{y}} \cdot (\mathbf{x}' - \mathbf{x}), \quad (11)$$

$$\begin{aligned} A_{ij}(\omega, s, \mathbf{x}, \mathbf{x}') &= \frac{\omega^4 J_{R_i}(\omega, s, \mathbf{x}) J_{R_j}(\omega, s, \mathbf{x}')}{(4\pi)^4 |\boldsymbol{\gamma}_i(s) - \mathbf{x}| |\boldsymbol{\gamma}_j(s) - \mathbf{x}'|} \\ &\times \frac{C_T(\omega, s, \mathbf{x}, \mathbf{x}')}{|\mathbf{x} - \mathbf{y}| |\mathbf{x}' - \mathbf{y}|}. \end{aligned} \quad (12)$$

$C_T(\omega, s, \mathbf{x}, \mathbf{x}')$ in (12) is a function related to the transmitted antenna beam pattern. If antenna beam pattern is known or can be approximated, $C_T(\omega, s, \mathbf{x}, \mathbf{x}') = J_T(\omega, \mathbf{x}) J_T^*(\omega, \mathbf{x}')$. If antenna beam pattern is unknown, but its covariance can be estimated, we can replace C_T with $C_T(\mathbf{x}, \mathbf{x}') = \mathbb{E}[J_T(\omega, \mathbf{x}) J_T^*(\omega, \mathbf{x}')] and redefine d_{ij} as $\mathbb{E}[d_{ij}]$ where \mathbb{E} denotes the expectation operator. If such information is not available, C_T can be set to $C_T \equiv 1$, corresponding to a non-informative prior on transmitter antenna beam pattern.$

We refer to \mathcal{F}_{ij} as the forward operator. Note that $\mathcal{F}_{ij} \approx \mathcal{L}_i \mathcal{L}_j^\dagger$, where \mathcal{L}_j^\dagger is the L^2 -adjoint of \mathcal{L}_j . Assuming a certain decay condition on A_{ij} , \mathcal{F}_{ij} becomes a Fourier integral operator (FIO). FIOs can be computed efficiently with the computational complexity of fast backprojection algorithms as described in [64].

Our objective is to recover \mathcal{R} or the *Kronecker scene* ρ from d_{ij} using the forward model \mathcal{F}_{ij} . Note that the mapping from $\tilde{\rho}$ to d_{ij} given in (5) is nonlinear. However,

$$d_{ij} = \mathcal{F}_{ij}[\mathcal{R}] \quad (13)$$

is linear. Note that once \mathcal{R} is recovered, the scene reflectivity $\tilde{\rho}$ can be obtained as the eigenvector of \mathcal{R} .

III. IMAGE FORMATION

A. Problem Formulation in Optimization Framework

The TDOA-based backprojection methods assume that the scene reflectivity satisfies the condition

$$\rho(\mathbf{x}, \mathbf{x}') = \tilde{\rho}(\mathbf{x}) \delta(\mathbf{x} - \mathbf{x}'). \quad (14)$$

This condition can be satisfied by an ideal point target. It can also be enforced statistically to a scene with a small number of point targets that are widely separated [9], [11]–[13], [43]. However, most SAR scenes have extended targets and complex geometric structures. Therefore, TDOA-based backprojection cannot produce an image of a typical SAR scene with good geometric fidelity.

In this paper, our objective is to form an image of $\tilde{\rho}$ using the model (10). Since $\rho : \mathbb{R}^2 \times \mathbb{R}^2 \rightarrow \mathbb{R}$ is the kernel of the rank-one positive semi-definite operator \mathcal{R} , the image formation problem lends itself to low-rank matrix recovery techniques [53], [55], [56].

Low-rank matrix recovery techniques have been developed as a generalization of matrix completion techniques [50], [51]; the difference being the constraint used. Rank minimization is a non-convex, NP-hard optimization problem. Typically, the nuclear norm is used as a convex relaxation for rank minimization [65], [66]. Furthermore, the nuclear norm minimization problem can be cast as a semi-definite program, and solved efficiently.

1) *Noise-free Measurement Case:* Let $\sigma_i(\mathcal{R})$ be the singular values of \mathcal{R} defined in (8).

Then the nuclear norm of \mathcal{R} (also known as the trace norm) is given by

$$\|\mathcal{R}\|_* = \sum_i |\sigma_i(\mathcal{R})|. \quad (15)$$

However, since in our problem \mathcal{R} is positive semi-definite, the singular values are also the eigenvalues, so the nuclear norm reduces to the trace of \mathcal{R} . Thus, we redefine (15) as

$$\|\mathcal{R}\|_* := \int \rho(\mathbf{x}, \mathbf{x}) d\mathbf{x} = \int |\tilde{\rho}(\mathbf{x})|^2 d\mathbf{x}. \quad (16)$$

In the case of noiseless measurements we formulate the image reconstruction as the following optimization problem:

$$\begin{aligned} & \text{minimize} && \|\mathcal{R}\|_* \\ & \text{subject to} && \mathcal{F}_{ij}[\mathcal{R}] = d_{ij} \\ & && \mathcal{R} \succeq 0, \quad \rho(\mathbf{x}, \mathbf{x}') \geq 0 \end{aligned} \quad (17)$$

where $\mathcal{R} \succeq 0$ denotes that \mathcal{R} is positive semi-definite.

2) *Noisy Measurement Case:* If the measurements are corrupted by noise, the received signal model at the i -th receiver becomes

$$d_i(\omega, s) = \mathcal{L}_i[\tilde{\rho}](\omega, s) + n_i(\omega, s), \quad i = 1, 2 \quad (18)$$

where \mathcal{L}_i is the bistatic forward operator, (1) and n_i , are the noise processes. We assume that $n_i(\omega, s)$ are zero-mean and statistically independent processes for $i \neq j$, and for all ω, s .³

Let

$$C_i(\omega, s; \omega', s') = \mathbb{E}[n_i(\omega, s)n_i^*(\omega', s')], \quad i = 1, 2. \quad (19)$$

The correlation of the received measurements, (4), with the addition of noise results in

$$d_{ij}(\omega, s) = \mathcal{F}_{ij}[\mathcal{R}](\omega, s) + \tilde{n}_{ij}(\omega, s) \quad i, j = 1, 2 \quad i \neq j \quad (20)$$

where

$$\begin{aligned} \tilde{n}_{ij}(\omega, s) = & \mathcal{L}_i[\tilde{\rho}](\omega, s)n_j^*(\omega, s) + \mathcal{L}_j[\tilde{\rho}]^*(\omega, s)n_i(\omega, s) \\ & + n_i(\omega, s)n_j^*(\omega, s) \quad i, j = 1, 2 \quad i \neq j. \end{aligned} \quad (21)$$

Since n_i and n_j are zero-mean, so is \tilde{n}_{ij} for all ω and s . Under the assumptions of statistical independence of n_i and n_j for $i \neq j$ for all ω, s , the covariance function C_{ij} of \tilde{n}_{ij} can be expressed as follows:

$$\begin{aligned} C_{ij}(\omega, s; \omega', s') = & \mathcal{F}_i[\mathcal{R}](\omega, s; \omega', s')C_j(\omega, s; \omega', s') \\ & + \mathcal{F}_j[\mathcal{R}](\omega, s; \omega', s')C_i(\omega, s; \omega', s') \\ & + C_i(\omega, s; \omega', s')C_j(\omega, s; \omega', s') \end{aligned} \quad (22)$$

$$i, j = 1, 2 \quad i \neq j$$

where $\mathcal{F}_i := \mathcal{L}_i\mathcal{L}_i^\dagger$, $i = 1, 2$. Since, we assume that $n_i(\omega, s)$ is zero-mean and statistically independent in ω, s , and $i \neq j$, $C_i(\omega, s; \omega', s') = 0$ and $C_j(\omega, s; \omega', s') = 0$ for $(\omega, s) \neq (\omega', s')$ and thus $C_{ij}(\omega, s; \omega', s') = 0$ for $(\omega, s) \neq (\omega', s')$. Then, under the assumption that $A_i(\omega, \mathbf{x}, \mathbf{y})$ and $A_j(\omega, \mathbf{x}, \mathbf{y})$ are approximately constant,

³We note that this assumption is satisfied if $n_i(t, s)$ are wide-sense stationary in fast-time t and statistically independent in slow-time and for $i \neq j$.

$\mathcal{F}_i[\mathcal{R}](\omega, s; \omega, s)$ and $\mathcal{F}_j[\mathcal{R}](\omega, s; \omega, s)$ are approximately proportional to $|\hat{\rho}(\omega(\hat{\gamma}_i(s) + \hat{\mathbf{y}}))|^2$ and $|\hat{\rho}(\omega(\hat{\gamma}_j(s) + \hat{\mathbf{y}}))|^2$ respectively where $\hat{\rho}$ is the Fourier transform of $\tilde{\rho}$ and $\hat{\gamma}(s)$ is the unit vector in the direction of $\gamma(s)$. For more details see **Appendix A**.

Let \mathcal{C} be an integral operator with the kernel C_{ij} defined by (22). We assume that \mathcal{C} is invertible and denote its inverse by \mathcal{C}^{-1} . Thus \mathcal{C} is positive definite and induces the norm

$$\begin{aligned} \|f\|_{\mathcal{C}^{-1}}^2 = \langle \mathcal{C}^{-1}f, f \rangle_{L^2} := & \int_{(\Omega \times S)^2} C_{ij}^{-1}(\omega, s; \omega', s')f(\omega', s') \\ & \times f^*(\omega, s)d\omega' ds' d\omega ds \end{aligned} \quad (23)$$

where C_{ij}^{-1} is the kernel of \mathcal{C}^{-1} .

Then, in the presence of noise, we can modify (17) by replacing the constraint with a weighted L^2 -norm, bounded by a threshold $\epsilon > 0$. Using the inverse of the covariance function serves as a whitening filter. This is also known as the generalized least squares criterion [67]. Thus, we state the image formation as the following optimization problem:

$$\begin{aligned} & \text{minimize} && \|\mathcal{R}\|_* \\ & \text{subject to} && \|\mathcal{F}_{ij}[\mathcal{R}] - d_{ij}\|_{\mathcal{C}^{-1}}^2 < \epsilon \\ & && \mathcal{R} \succeq 0, \quad \rho(\mathbf{x}, \mathbf{x}') \geq 0. \end{aligned} \quad (24)$$

B. Optimization Method for Image Reconstruction

In order to solve the optimization problems (17) and (24), we use an approach similar to one described in [53], [55]. We reformulate (17) and (24) as

$$\begin{aligned} & \text{minimize} && g(\rho) = \frac{1}{2} \|\mathcal{F}_{ij}[\mathcal{R}] - d_{ij}\|_{\mathcal{Q}}^2 + \lambda \|\mathcal{R}\|_* \\ & \text{subject to} && \mathcal{R} \succeq 0, \quad \rho(\mathbf{x}, \mathbf{x}') \geq 0 \end{aligned} \quad (25)$$

where $\lambda > 0$ is the regularization parameter and \mathcal{Q} is equal to the identity operator for the noise-free case and to \mathcal{C}^{-1} for the noisy case.

For the noisy case, this formulation is equivalent to the original problem with the proper choice of regularization parameter λ that is related to ϵ . For the noise-free case, (17) can be solved via semi-definite programming after discretizing the problem. However, semi-definite programming does not scale well with respect to the number of dimensions. Hence, we solve (17) approximately using (25). This approach has the advantage of computational efficiency at the expense of a trade-off between the trace minimization and constraint satisfaction.

We solve (25) using an algorithm based on Nesterov gradient-based iterative approach [55], [56], [60]. First, we discretize and vectorize the Kronecker scene ρ and data d_{ij} to form vectors $\boldsymbol{\rho}$ and \mathbf{d} , respectively. In the discrete setting we represent the linear integral operators \mathcal{F}_{ij} , \mathcal{Q} , \mathcal{K} as matrices by discretizing their kernels. These matrices are denoted by \mathbf{F} , \mathbf{Q} and \mathbf{K} , respectively. The matrix \mathbf{F} is formed, such that, when multiplied by $\boldsymbol{\rho}$, the correlated data vector \mathbf{d} results. For noiseless measurements \mathbf{Q} is the identity matrix and the inverse of the covariance matrix in the noisy case. Appendix A

describes in more detail the form that \mathbf{Q} takes for noisy case. Then, \tilde{g} , the discrete approximation of g , becomes

$$\tilde{g}(\boldsymbol{\rho}) = \frac{1}{2}(\mathbf{F}\boldsymbol{\rho} - \mathbf{d})^H \mathbf{Q}(\mathbf{F}\boldsymbol{\rho} - \mathbf{d}) + \lambda \text{Tr}(\text{mat}(\boldsymbol{\rho})), \quad (26)$$

where $\text{mat}(\boldsymbol{\rho})$ converts $\boldsymbol{\rho}$ into a matrix corresponding to the operator \mathcal{R} . Tr denotes the trace operator. The algorithm is initialized using an image obtained by backprojecting the correlated data using the following filtered-backprojection (FBP) operator:

$$p(\mathbf{z}, \mathbf{z}') := \mathcal{K}[d](\mathbf{z}, \mathbf{z}') = \int e^{-i2\pi\omega r_{ij}(s, \mathbf{z}', \hat{\mathbf{y}})} B_{ij}(\omega, \mathbf{z}, \mathbf{z}', \mathbf{y}) \times d(\omega, s) d\omega ds, \quad (27)$$

where the filter, B_{ij} is of the form [68]

$$B_{ij}(\omega, s, \mathbf{z}, \mathbf{z}', \mathbf{y}) \propto \frac{A_{ij}^*(\omega, \mathbf{z}, \mathbf{z}', \mathbf{y})}{|A_{ij}(\omega, \mathbf{z}, \mathbf{z}', \mathbf{y})|}. \quad (28)$$

The operator \mathcal{K} is related to the L^2 -adjoint of \mathcal{F}_{ij} . We outline the initialization and iteration steps of the algorithm as follows:

- 1) *Initialization*: The iteration starts with the \mathbf{p}_0 reconstructed by the FBP operator given in (27), $\mathbf{p}_0 = \mathbf{K}\mathbf{d}$, where \mathbf{K} is the discretized FBP operator. The initial Kronecker image is then given by $\boldsymbol{\rho}_0 = \mathbf{p}_0$.
- 2) *Iteration*: The k -th update of the Kronecker scene is given by

$$\hat{\boldsymbol{\rho}}_k = \text{vec}[\mathcal{P}(\text{mat}(\mathbf{p}_{k-1} - \alpha_k \nabla \tilde{g}(\mathbf{p}_{k-1})))] \quad (29)$$

where $\{\alpha_k\}$ is the step sequence, vec vectorizes its matrix argument, and

$$\mathcal{P}(\mathbf{A}) = \sum_k \max(\lambda_k, 0) \mathbf{u}_k \otimes \mathbf{u}_k^*. \quad (30)$$

In (30), \mathbf{u}_k 's are the eigenvectors of \mathbf{A} and λ_k are the corresponding eigenvalues of \mathbf{A}^4 . Note that by (26),

$$\nabla \tilde{g}(\mathbf{z}) = \mathbf{F}^H \mathbf{Q}(\mathbf{F}\mathbf{z} - \mathbf{d}) + \lambda \text{vec}(\mathbf{I}) \quad (31)$$

where \mathbf{I} is the identity matrix. From the equation above, we see that $\nabla \tilde{g}$ involves the adjoint of the forward operator \mathcal{F}_{ij} , which, in our implementation is approximated by the filtered-backprojection operator, \mathcal{K} given in (27).

The iteration in (29) is a projected gradient descent. The iteration moves in the direction of the gradient of (26) and projects the result onto the positive semi-definite cone, enforcing the positive definiteness constraint. We now summarize the algorithm as outlined above in **Algorithm 1**

Note that the sequences $\{\theta\}_n, \{\beta\}_n$ are sequences that accelerate the convergence [56], [61].

IV. COMPUTATIONAL COMPLEXITY

Assuming there are $\mathcal{O}(N)$ samples in both the fast- and slow-time variables, and the scene is sampled according to $\mathcal{O}(N \times N)$, the computational complexity of the main loop of **Algorithm 1** breaks down as follows:

⁴ \mathcal{P} is the projects a matrix onto its positive semi-definite cone.

Algorithm 1

Input: $\mathbf{p}_0, \mathbf{d}, \lambda, \{\alpha_k\}$

- 1: $\hat{\boldsymbol{\rho}}_0 \leftarrow \mathbf{p}_0, \theta_0 \leftarrow 1, k \leftarrow 1$
 - 2: **repeat**
 - 3: $\hat{\boldsymbol{\rho}}_k \leftarrow \text{vec}[\mathcal{P}(\text{mat}(\mathbf{p}_{k-1} - \alpha_k \nabla \tilde{g}(\mathbf{p}_{k-1})))]$
 - 4: $\theta_k \leftarrow 2 \left(1 + \sqrt{1 + 4/\theta_{k-1}^2}\right)^{-1}$
 - 5: $\beta_k \leftarrow \theta_k(\theta_{k-1}^{-1} - 1)$
 - 6: $\mathbf{p}_k \leftarrow \hat{\boldsymbol{\rho}}_k + \beta_k(\hat{\boldsymbol{\rho}}_k - \hat{\boldsymbol{\rho}}_{k-1})$
 - 7: $k \leftarrow k + 1$
 - 8: **until** stopping criteria is met
-

- 1) *Correlate received measurements* (4): This can be carried out in the frequency domain; The Fourier transform in fast-time can be carried out using FFT requiring $\mathcal{O}(N \log N)$ operations, for each slow-time. For all slow time samples s , the total computational complexity of this step is $\mathcal{O}(N^2 \log N)$.
- 2) *Form initial image $\hat{\rho}$ using filtered-backprojection*: We form an initial image based on (27) using the filter B_{ij} to compensate for the known amplitude terms. One can carry out this operation using backprojection method. Since the Kronecker scene, ρ is $\mathcal{O}(N^2 \times N^2)$, the operation takes $\mathcal{O}(N^8)$ operations. If the fast backprojection algorithm is used, the computational complexity of this step can be reduced to $\mathcal{O}(N^4 \log N)$ [69].
- 3) *Calculate ∇g , the gradient of the objective functional g* : The first step of the **Algorithm 1** is a gradient descent procedure and requires the calculation of $\nabla \tilde{g}(\mathbf{p}_k)$. The computational complexity of this step is dominated by the forward-projection of \mathbf{p}_k using (10) and the back-projection of the residual. Calculation of the forward projection requires a multiplication of $\mathcal{O}(N^2 \times N^4)$ matrix by $\mathcal{O}(N^4)$ vector, which results in $\mathcal{O}(N^6)$ operations. This can be improved using the fast FIO computation algorithm of Candes et. al. in [64] which reduces the computational complexity to $\mathcal{O}(N^5 \log N)$. This is followed by the backprojection step, which, as mentioned in the second step of the algorithm, requires $\mathcal{O}(N^4 \log N)$ operations using fast backprojection algorithm. Thus, this step has the computational complexity of $\mathcal{O}(N^5 \log N)$ if fast FIO and fast backprojection algorithms are used.
- 4) *Projection onto semi-definite cone* (30): This step requires eigendecomposition of the current Kronecker image estimate, $\hat{\boldsymbol{\rho}}_k$. The computational complexity of the eigenvalue decomposition of $\mathcal{O}(N^2 \times N^2)$ matrix is $\mathcal{O}(N^6)$.
- 5) *Update $\hat{\rho}$* : This step involves a few arithmetic operations and scalar multiplication, making the computational complexity of this step negligible.
- 6) *Image formation*: Repeat Steps 3 through 5 until convergence or a maximum number of iterations is reached. Form the final image by keeping the largest eigenvalue/eigenvector of $\hat{\rho}$.

Thus, the main loop has the computational complexity of $\mathcal{O}(N^6)$ if fast backprojection and fast FIO algorithms are

utilized. Otherwise, the complexity of each iteration may be as much as $\mathcal{O}(N^8)$. Without further analysis on the convergence behavior of the algorithm - which is outside the scope of the present work - we cannot make conclusions on the convergence rate. However, we note that we have observed, experimentally, that the algorithm tends to converge rather quickly as compared to the dimensions of the Kronecker scene, N^2 ; typically in the order of 10s of iterations, even when N is significantly large.

Compared to the computational complexity of the traditional TDOA backprojection under incoherent field approximation - which may be as low as $\mathcal{O}(N^2 \log N)$ using fast backprojection algorithms - there is a cost of increased computational complexity to gain the accuracy of reconstructing complex extended targets provided by the new algorithm. It should be noted, however, that the majority of the calculations within each iteration can be naturally parallelized. For instance, in the forward- and backprojection steps, one can compute each s sample in parallel as the computations are independent of each other.

V. NUMERICAL SIMULATIONS

To demonstrate the performance of our new imaging method, we perform extensive numerical simulations. We conduct several sets of experiments involving point targets and extended targets and compare the performance of our method with that of TDOA backprojection. Additionally, we numerically investigate the robustness of our method to additive noise and phase errors resulting from incorrect transmitter location information.

We consider a scenario with two receivers on a circular trajectory looking down on a square scene with a single stationary transmitter located away from the scene. The receivers traverse the same circular trajectory $\gamma(s) = (10 \cos(s), 10 \sin(s), 6)\text{km}$, in tandem separated by $\pi/4$ radians. The transmitter is stationary and located at $(15, 15, 3)\text{km}$. Figure 2 illustrates this scenario. We assume that the transmitted waveform has a center frequency of 760MHz with 8MHz bandwidth. We set J_T and J_R to 1, and generate the data, d_{ij} by correlating the bistatic measurements simulated based on (1). We synthesized 128 slow-time samples along the circular trajectory, and 64 fast-times samples at each slow-time.

We assume the topography is flat and the scene is $[0, 400] \times [0, 400]\text{m}^2$ discretized into 16×16 pixels. Note that this requires recovering a Kronecker scene of 256×256 , with significantly larger unknowns than the 16×16 scene reflectivity.

We form images by solving (25) using the iteration in **Algorithm 1**.

There are two tuning parameters in line 3 of **Algorithm 1**, specifically, the regularization parameter λ and the step size sequence $\{\alpha_k\}$. During our experiments we noticed that the ℓ^2 norm of the image resulting from backprojection of the residual may vary largely from one iteration to the next. In order to minimize the rank and ensure that (24) is equivalent to (25), the trace term in the objective function should dominate. To deal with this variation, we use an adaptive value of λ , and define it as

$$\lambda_k = 2.5 \max \{ |\mathbf{K}\mathbf{Q}_k(\mathbf{F}\boldsymbol{\rho}_k - \mathbf{d}_k)| \}, \quad (32)$$

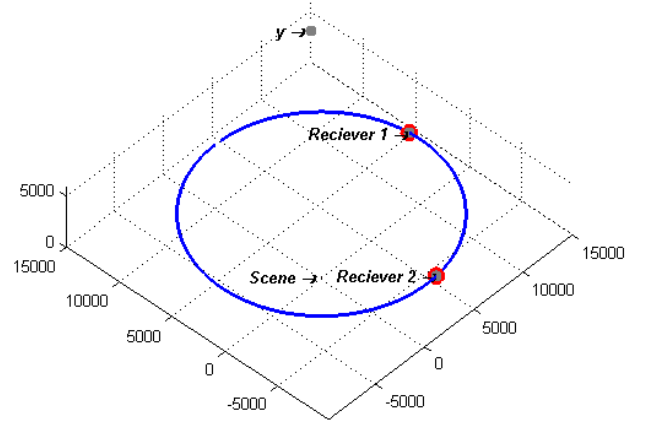


Fig. 2. Set up for simulations. The receivers traverse circular trajectory with radius 10km, while the transmitter is stationary outside the scene. The scene is size $[400 \times 400]\text{m}$.

where \mathbf{K} is the matrix representation of the filtered-backprojection operator (27). A constant step size, $\alpha = 1\text{e}6$ is used in all of our simulations.

A. Performance of TDOA and LRMR Methods for Point and Extended Targets

We compare the performance of our LRMR imaging method with that of TDOA backprojection [9] for two scenes, each one consisting of extended or point targets shown in Figure 3. The extended target scene shown in Figure 3(a) consists of two overlapping extended targets. Imaging this scene requires reconstruction of three different reflectivity values, specifically, 0.33 in the region $[100, 250] \times [175, 300]\text{m}^2$, 0.66 in $[200, 300] \times [75, 200]\text{m}^2$, and 1 in $[200, 250] \times [175, 200]\text{m}^2$. The distributed point target scene is shown in Figure 3(b). It consists of 5 point targets with unit reflectivity located at: $(250, 100)\text{m}$, $(100, 150)\text{m}$, $(200, 225)\text{m}$, $(150, 300)\text{m}$, $(325, 350)\text{m}$.

The images formed using our method are shown in Figures 3(c) and 3(d). The images formed by the TDOA backprojection are shown in Figures 3(e) and 3(f). It is clear that our method improves upon the TDOA backprojection method drastically for both the extended and distributed point target cases. Comparison of Figures 3(c) and 3(e) show that the incoherent field assumption breaks down for extended targets and TDOA backprojection attempts to reduce the extended target to a point target. Similarly, for the distributed point target case, LRMR produces an image with better background suppression than that of TDOA backprojection. Our method reconstructs targets at or close to the correct magnitude. Additionally, in the TDOA backprojection images, targets are difficult to distinguish from the background. In both cases we see that our method produces images with better geometric fidelity, sharper edges and superior background attenuation.

Since our new imaging method reconstructs the Kronecker scene and extracts the scene reflectivity from the top eigen-

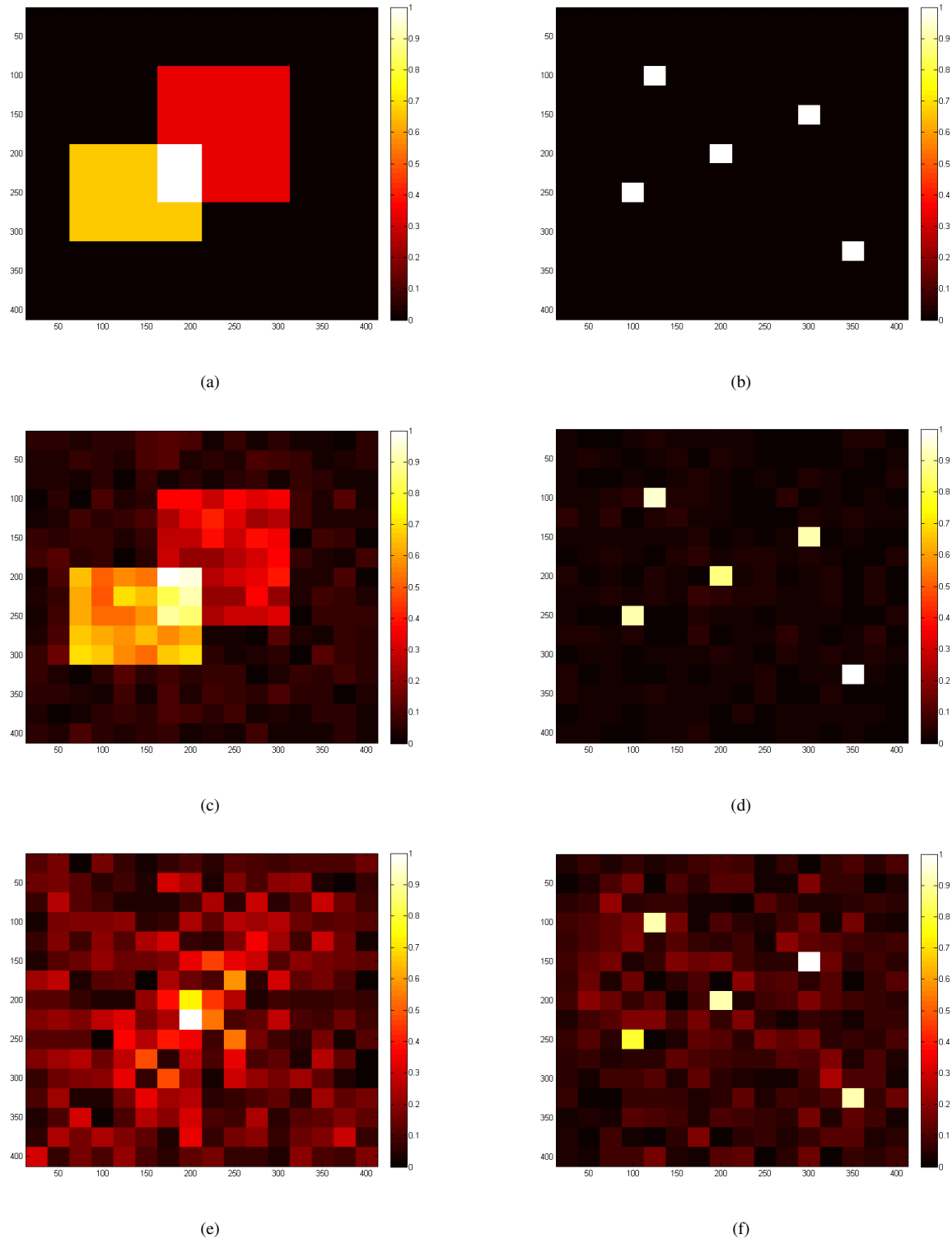


Fig. 3. (a) Original extended target scene. (b) Original point target scene. (c) Extended target scene reconstructed using low-rank matrix recovery methods. (d) Point target scene reconstructed using low-rank matrix recovery methods. (e) The reconstructed extended scene image using TDOA backprojection. (f) Reconstructed point target image using TDOA backprojection.

vector of the estimated Kronecker scene, we compare the original and estimated Kronecker scenes for the extended target case in Figure 4. The Kronecker image is estimated after 15 iterations of **Algorithm 1**. A visual comparison of the reconstructed image shows good agreement with the original

Kronecker scene.

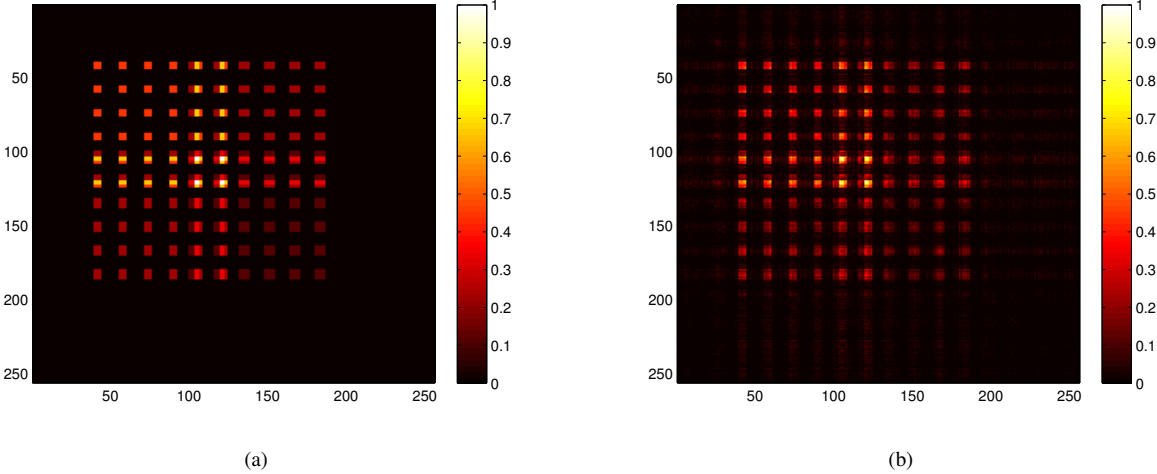


Fig. 4. The solution to (17) will be the Kronecker product of the reconstructed scene. (a) The original Kronecker product scene. (b) The reconstruction of figure (a).

B. Robustness of LRMR Imaging wrt to Transmitter Location Uncertainty

The knowledge of transmitter locations may be uncertain for variety of reasons: in some cases, it may be unknown or deviate from its true position. For example, a television station with an elevated antenna can sway due to wind. This can result in phase errors in the reconstruction process. In this subsection we perform numerical simulations to evaluate the robustness of our method with respect to errors in transmitter location.

We perturb \mathbf{y} , the true location of the transmitter, with ϵ . Specifically, we synthesize bistatic measurements based on the true location of the transmitter \mathbf{y} , but reconstruct LRMR images using the unit vector direction corresponding to $\mathbf{y} + \epsilon = [y_1 + \epsilon_1, y_2 + \epsilon_2, y_3 + \epsilon_3]$. Each component of ϵ is i.i.d. Gaussian with variance of 1 km, i.e. $\epsilon \sim \mathcal{N}(0, 1)$. This scenario corresponds to the case, for example, when the antenna sways from its known position. Next we assume that ϵ has non-zero mean. This scenario corresponds to a case in which the location of the transmitter is poorly estimated.

For these experiments we use the extended target scene displayed in figure 5(a). All experiments in this subsection use 9 iterations. The remaining parameters are kept the same as in the previous subsection. The scene used for these experiments consists of two regions that correspond to $[100, 325] \times [100, 325]\text{m}^2$ with 0.5 reflectivity value and $[175, 175] \times [225, 225]\text{m}^2$ with unit reflectivity; the scene is displayed in Figure 5(a). Figure 5 displays the images reconstructed for $\epsilon = 0$ which corresponds to the the correct transmitter location. The LRMR reconstruction is shown in figure 5(b) and the TDOA backprojection image in figure 5(c). Once again, we see that the LRMR method reconstructs complicated scenes consisting of extended targets with high fidelity, whereas TDOA based backprojection clearly fails.

Figure 6 shows an image reconstructed using the LRMR method for a single realization of ϵ centred at the true transmitter location. This demonstrates that for a stationary transmitter, variation of up to 1-2 km will have negligible effect on the reconstructed image. Using 10 realizations of

ϵ we compute the mean square error (MSE) between the LRMR reconstructed images and the true scene. We find the error is negligible (approximately 0.00003), demonstrating the robustness of our method with respect to phase error that can result from movement of elevated antennas.

We consider next phase error resulting from incorrect knowledge of the transmitter location. To investigate the effect of incorrect antenna location we consider 25 locations forming a grid over the region $[5, 5, 3] \times [25, 25, 3]\text{km}^2$, spaced 5km apart, along the (x_1, x_2) plane. The true location and erroneous locations of the transmitter are shown in Figure 7(a). Using 5 realizations of ϵ for each location, we form a surface plot of MSE, shown in Figure 7(b). It is apparent from the figure that there is local minima in the locations of \mathbf{y} where the illumination direction remains constant.

C. Robustness of LRMR and TDOA based Imaging wrt Additive Noise

We consider the extended target and the distributed point target scenes described in subsection V-A and shown in Figure 3(a) and 3(b). To simulate noisy data, we first generate noise-free signal using (1) and next add white noise at different signal-to-noise ratios (SNR). We then correlate the noisy measurements to form (20). We formed the LRMR and TDOA backprojection images at SNR values ranging from 0dB to 10dB. The mean square error for each SNR value was calculated out of ten realizations of noise.

In the case of the extended target scene, reconstructed LRMR images are shown in Figure 8 at two different SNR levels based on a single realization of additive noise. For TDOA backprojection, the reconstructed image in the noise-free case is of unacceptable quality (see Figure 3(e)), in the presence of noise the resolution degrades even further. Figure 9 shows an image formed using TDOA backprojection for a single realization of noise, the addition of noise further degrades the foreground-to-background ratio. Realizations for an SNR level of 4dB and 0dB are shown in figures 9(a) and 9(b), respectively. The LRMR image formed using a single

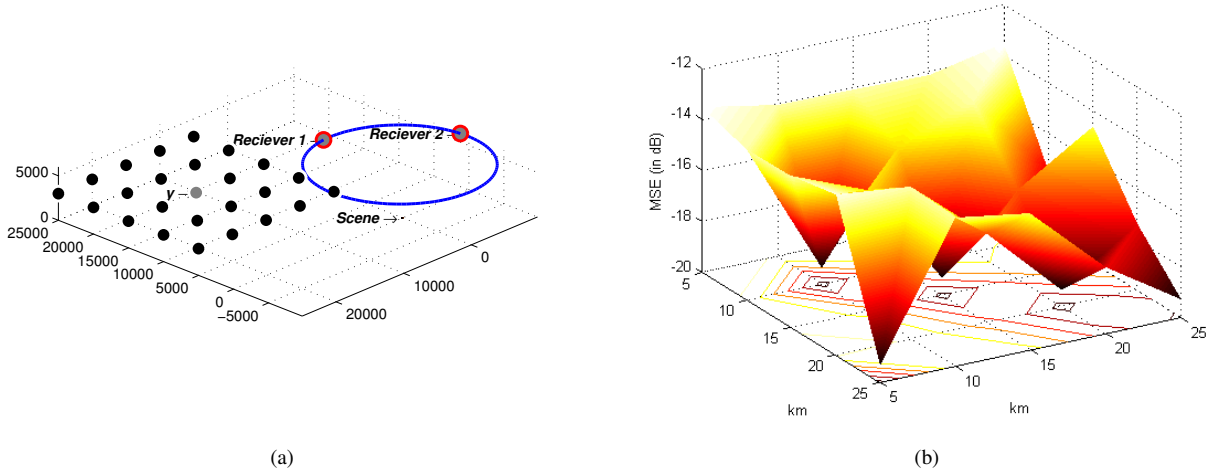


Fig. 7. The transmitter locations \mathbf{y} and the resulting MSE between the LRMR images reconstructed with true transmitter direction and erroneous directions. (a) The imaging configuration and transmitter locations used. The gray dot indicates the true \mathbf{y} , while the black dots indicate the erroneous locations we consider. (b) A plot of the MSE error, measurement points correspond to those in Figure (a).

realization of noise at SNR value of 4dB, is shown in Figure 8(a). The reconstructed image for this level of noise still possesses good geometric fidelity, the only negative effect of noise appears in greater variation in pixel intensity, specifically in the objects of interest. At the SNR level of 0dB, the reconstructed image exhibits noticeable deterioration, however, some structural information about the edges is still present, as seen in Figure 8(b).

Figures 10 and 11 show the MSE versus SNR for the extended and distributed point target scenes, respectively. For both scenes, we see that the TDOA backprojection results in a significantly larger MSE than that of the new method. The MSE of our method increases at a faster rate for SNR levels of 3dB and lower, however, it still remains significantly lower than that of TDOA backprojection. For 0dB SNR level, we see that our method improves over TDOA backprojection by 6dB and at 10dB SNR level the improvement is 12dB for the extended and 8dB for the distributed point target cases.

VI. CONCLUSION

We present a new method that overcomes many of the limitations of the TDOA based backprojection for passive SAR imaging. TDOA based reconstruction is ideal for point targets. For multiple point targets, it results in spurious ghost targets. Furthermore, it fails to reconstruct extended targets with acceptable image quality. The new method can reconstruct heterogeneous scenes and extended targets with good geometric fidelity and sharp edges. Furthermore, it does not require the locations of transmitters of opportunity and exhibit robustness with respect to phase errors.

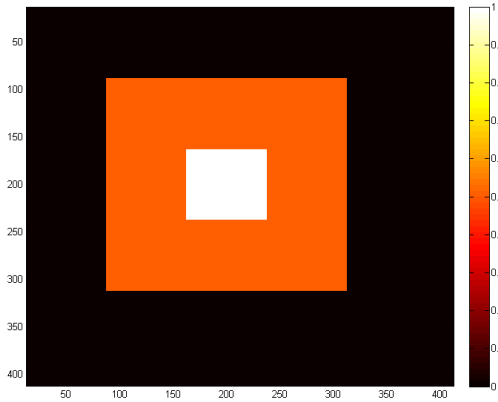
Our image formation method is based on the observation that the correlation of bistatic measurements results in a forward model that maps an unknown positive semi-definite, rank-one operator to correlated measurements. This allows us to formulate the image formation in the low-rank matrix recovery framework. The scene reflectivity is simply the eigenvector of the unknown positive semi-definite, rank-one operator,

which we refer to as the Kronecker scene or image. We take into account additive noise in bistatic measurements and formulate the image reconstruction as a convex optimization problem with a constraint on the rank of the Kronecker image. We present an algorithm to address the convex optimization problem based on Nesterov gradient-based iteration. We obtain the scene reflectivity as the eigenvector of the estimated Kronecker image. We analyze the computational complexity of the iterative algorithm. The analysis shows that the new algorithm has a higher computational complexity than that of TDOA based backprojection. However, the structure of the algorithm is amenable to parallel implementation. The reconstruction method is non-linear and hence, does not lend itself to a straightforward resolution analysis. We leave the task of analyzing the resolution of the method for the future.

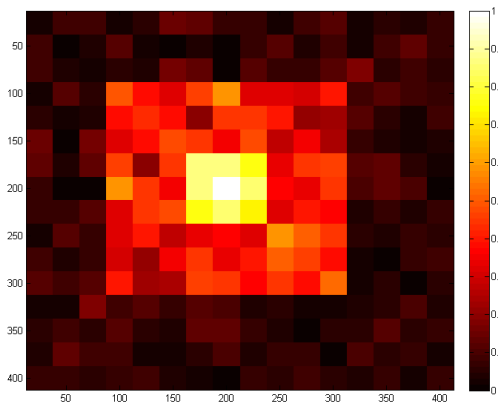
Extensive numerical simulations show that the new method is superior to TDOA for the extended targets and distributed point targets. In this work, we specifically considered passive SAR imaging of a stationary scene. However, the method can be extended to include passive imaging of moving scenes, Doppler based imaging and passive multi-static imaging using stationary and moving antennas [6], [11]–[13], [19], [43], [70].

REFERENCES

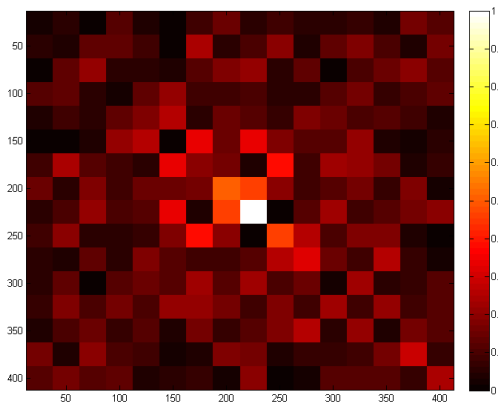
- [1] Q. Wang, Y. Lu, and C. Hou, "An experimental WiMAX based passive radar study," pp. 1204–1207, Dec 2009.
- [2] H. Griffiths and C. Baker, "Passive coherent location radar systems. part 1: performance prediction," *Radar, Sonar and Navigation, IEEE Proceedings* -, vol. 152, no. 3, pp. 153–159, June 2005.
- [3] C. Baker, H. Griffiths, and I. Papoutsis, "Passive coherent location radar systems. part 2: waveform properties," *Radar, Sonar and Navigation, IEEE Proceedings* -, vol. 152, no. 3, pp. 160–168, June 2005.
- [4] B. Dawidowicz, P. Samczynski, M. Malanowski, J. Misiurewicz, and K. Kulpa, "Detection of moving targets with multichannel airborne passive radar," *Aerospace and Electronic Systems Magazine, IEEE*, vol. 27, no. 11, pp. 42–49, November 2012.
- [5] P. Krysiak and K. Kulpa, "The use of a GSM-based passive radar for sea target detection," in *Radar Conference (EuRAD), 2012 9th European*, Oct 2012, pp. 142–145.
- [6] L. Wang, I.-Y. Son, and B. Yazici, "Passive imaging using distributed apertures in multiple-scattering environments," *Inverse Problems*, vol. 26, no. 6, p. 065002, 2010.



(a)



(b)

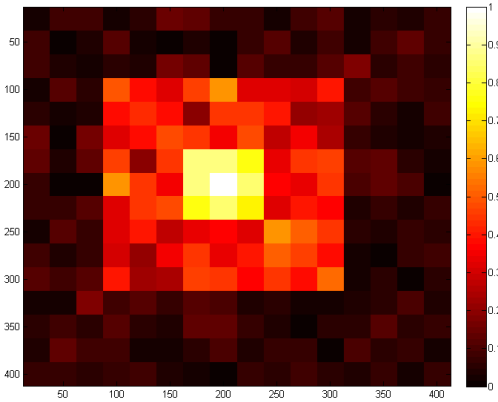


(c)

Fig. 5. The scene used for transmitter uncertainty experiments and reconstructions corresponding to $\epsilon = 0$. (a) The original scene. (b) The reconstructed image using the LRMR method. (c) The image formed using TDOA backprojection.

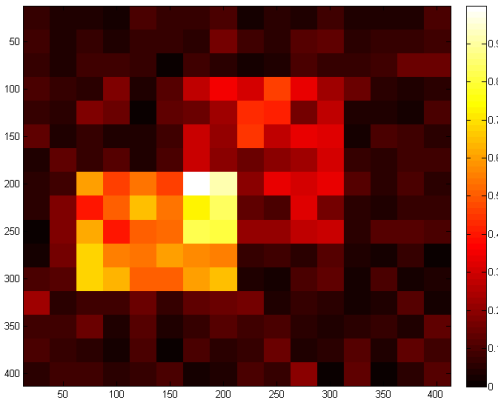
[7] M. Rapson, "Passive multistatic radar imaging using an OFDM based signal of opportunity," Ph.D. dissertation, Air Force Institute of Technology, 2012.

[8] J. Palmer, H. Harms, S. Searle, and L. Davis, "DVB-T passive radar signal processing," *Signal Processing, IEEE Transactions on*, vol. 61,

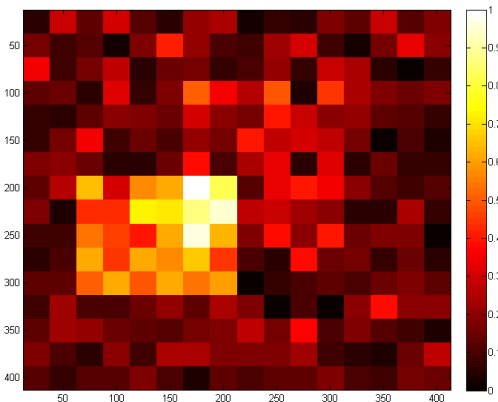


(a)

Fig. 6. An image formed using a single realization of ϵ centred around the true location. The value of \hat{y} is calculated using the vector $y = [y_1 + \epsilon_1, y_2 + \epsilon_2, y_3 + \epsilon_3]$ for $\epsilon \sim \mathcal{N}(0, 1)$.

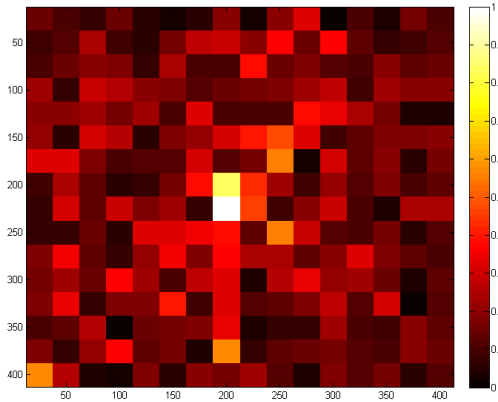


(a)

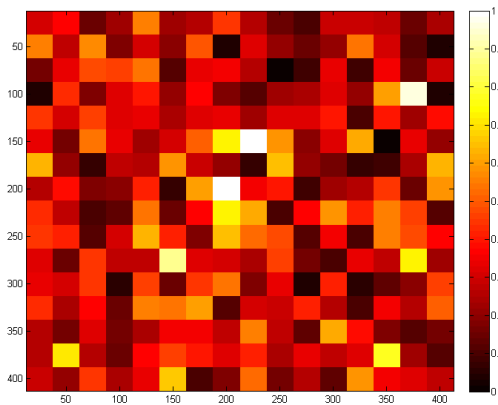


(b)

Fig. 8. Images formed using the LRMR method for a single realization of noise are shown for two SNR values. (a) The reconstructed image for a SNR level of 4dB. (b) The reconstructed image for a SNR level of 0dB.

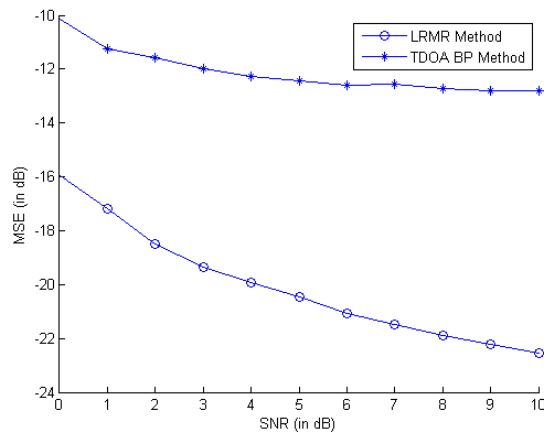


(a)



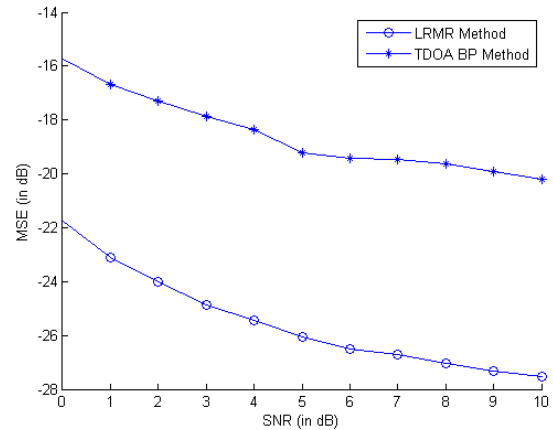
(b)

Fig. 9. Images formed using the TDOA backprojection method for a single realization of noise are shown for two SNR values. (a) The reconstructed image for a SNR level of 4dB. (b) The reconstructed image for a SNR level of 0dB.



(a)

Fig. 10. The MSE curve for SNR values ranging from 0dB to 10dB recorded in increments of 1dB for the extended target scene. The bottom curve is the result of the LRMR method, and the top curve is the TDOA backprojection method.



(a)

Fig. 11. The MSE curve for SNR values ranging from 0dB to 10dB recorded in increments of 1dB for the point target scene. The bottom curve is the result of the LRMR method, and the top curve is the TDOA backprojection method.

- [9] C. Yarman and B. Yazici, "Synthetic aperture hitchhiker imaging," *IEEE Transactions on Imaging Processing*, pp. 2156–2173, 2008.
- [10] D. Hack, L. Patton, A. Kerrick, and M. Saville, "Direct cartesian detection, localization, and de-ghosting for passive multistatic radar," in *Sensor Array and Multichannel Signal Processing Workshop (SAM), 2012 IEEE 7th*, June 2012, pp. 45–48.
- [11] L. Wang, C. Yarman, and B. Yazici, "Doppler-Hitchhiker: A novel passive synthetic aperture radar using ultranarrowband sources of opportunity," *Geoscience and Remote Sensing, IEEE Transactions on*, vol. 49, no. 10, pp. 3521–3537, Oct 2011.
- [12] C. Yarman, L. Wang, and B. Yazici, "Doppler synthetic aperture hitchhiker imaging," *Inverse Problems*, vol. 26, no. 6, p. 065006, 2010. [Online]. Available: <http://stacks.iop.org/0266-5611/26/i=6/a=065006>
- [13] S. Wacks and B. Yazici, "Passive synthetic aperture hitchhiker imaging of ground moving targets - part 1: Image formation and velocity estimation," *Image Processing, IEEE Transactions on*, vol. 23, no. 6, pp. 2487–2500, June 2014.
- [14] D. Hack, L. Patton, B. Himed, and M. Saville, "Centralized passive MIMO radar detection without direct-path reference signals," *Signal Processing, IEEE Transactions on*, vol. 62, no. 11, pp. 3013–3023, June 2014.
- [15] L. Wang and B. Yazici, "Bistatic synthetic aperture radar imaging using narrowband continuous waveforms," *Image Processing, IEEE Transactions on*, vol. 21, no. 8, pp. 3673–3686, Aug 2012.
- [16] J. Garnier and G. Papanicolaou, "Passive sensor imaging using cross correlations of noisy signals in a scattering medium," *SIAM Journal on Imaging Sciences*, vol. 2, no. 2, pp. 396–437, 2009.
- [17] J. Garnier, G. Papanicolaou, A. Semin, and C. Tsogka, "Signal-to-noise ratio estimation in passive correlation-based imaging," *SIAM Journal on Imaging Sciences*, vol. 6, no. 2, pp. 1092–1110, 2013.
- [18] L. Wang and B. Yazici, "Passive imaging of moving targets using sparse distributed apertures," *SIAM Journal on Imaging Sciences*, vol. 5, no. 3, pp. 769–808, 2012.
- [19] —, "Passive imaging of moving targets exploiting multiple scattering using sparse distributed apertures," *Inverse Problems*, vol. 28, no. 12, p. 125009, 2012.
- [20] H. Ammari, J. Garnier, and W. Jing, "Passive array correlation-based imaging in a random waveguide," *Multiscale Modeling & Simulation*, vol. 11, no. 2, pp. 656–681, 2013.
- [21] L. Maslikowski, P. Samczynski, M. Baczyk, P. Krysiak, and K. Kulpa, "Passive bistatic SAR imaging - challenges and limitations," *Aerospace and Electronic Systems Magazine, IEEE*, vol. 29, no. 7, pp. 23–29, July 2014.
- [22] H. Wuming and W. Jun, "Airborne SAR passive radar imaging algorithm based on external illuminator," in *Synthetic Aperture Radar, 2007. APSAR 2007. 1st Asian and Pacific Conference on*, Nov 2007, pp. 642–645.
- [23] M. Cetin and A. Lanterman, "Region-enhanced passive radar imaging,"

- Radar, Sonar and Navigation, IEEE Proceedings* -, vol. 152, no. 3, pp. 185–194, June 2005.
- [24] K. Suwa, S. Nakamura, S. Morita, T. Wakayama, H. Maniwa, T. Oshima, R. Maekawa, S. Matsuda, and T. Tachihara, “ISAR imaging of an aircraft target using ISDB-T digital TV based passive bistatic radar,” in *Geoscience and Remote Sensing Symposium (IGARSS), 2010 IEEE International*, July 2010, pp. 4103–4105.
- [25] V. Kubica and X. Neyt, “Passive SAR imaging using the asar instrument of ENVISAT as transmitter of opportunity,” in *Synthetic Aperture Radar, 2012. EUSAR. 9th European Conference on*, April 2012, pp. 275–278.
- [26] P. Samczynski and K. Kulpa, “Passive SAR imaging using a satellite pulsed radar as an illuminator of opportunity,” in *Radar Symposium (IRS), 2012 13th International*, May 2012, pp. 157–161.
- [27] K. Kulpa, P. Samczynski, M. Malanowski, L. Maslikowski, and V. Kubica, “The use of CLEAN processing for passive SAR image creation,” in *Radar Conference (RADAR), 2013 IEEE*, April 2013, pp. 1–6.
- [28] A. Evers and J. Jackson, “Experimental passive SAR imaging exploiting LTE, DVB, and DAB signals,” in *Radar Conference, 2014 IEEE*, May 2014, pp. 0680–0685.
- [29] R. Takahashi, K. Hirata, and A. Okamura, “Subband cross-correlation processing with interference mitigation for passive bistatic radar,” in *Radar Conference, 2014 IEEE*, May 2014, pp. 0573–0578.
- [30] P. Krysik, L. Maslikowski, P. Samczynski, and A. Kurowska, “Bistatic ground-based passive SAR imaging using TerraSAR-X as an illuminator of opportunity,” in *Radar (Radar), 2013 International Conference on*, Sept 2013, pp. 39–42.
- [31] M. Antoniou and M. Cherniakov, “Experimental demonstration of passive GNSS-based SAR imaging modes,” in *Radar Conference 2013, IET International*, April 2013, pp. 1–5.
- [32] W.-Q. Wang, J. Cai, and Q. Peng, “Near-space SAR: A revolutionary microwave remote sensing mission,” in *Synthetic Aperture Radar, 2007. APSAR 2007. 1st Asian and Pacific Conference on*, Nov 2007, pp. 127–131.
- [33] P. Samczynski, K. Kulpa, M. Malanowski, P. Krysik, and L. Maslikowski, “Trial results on passive SAR measurement using the ENVISAT-1 satellite as an illuminator of opportunity,” in *Synthetic Aperture Radar, 2012. EUSAR. 9th European Conference on*, April 2012, pp. 291–294.
- [34] C. Prati, F. Rocca, D. Giancola, and A. Guarnieri, “Passive geosynchronous SAR system reusing backscattered digital audio broadcasting signals,” *Geoscience and Remote Sensing, IEEE Transactions on*, vol. 36, no. 6, pp. 1973–1976, Nov 1998.
- [35] W.-Q. Wang, “Near-space passive remote sensing for homeland security: Potential and challenges,” *parameters*, vol. 2, pp. 1021–1028, 2008.
- [36] D. Pastina, M. Sedehi, and D. Cristallini, “Passive bistatic ISAR based on geostationary satellites for coastal surveillance,” in *Radar Conference, 2010 IEEE*, May 2010, pp. 865–870.
- [37] B. Mojarabi, J. Homer, K. Kubik, and I. Longstaff, “Power budget study for passive target detection and imaging using secondary applications of GPS signals in bistatic radar systems,” in *Geoscience and Remote Sensing Symposium, 2002. IGARSS '02. 2002 IEEE International*, vol. 1, 2002, pp. 449–451 vol.1.
- [38] D. Gromek, P. Krysik, K. Kulpa, P. Samczynski, and M. Malanowski, “Ground-based mobile passive imagery based on a DVB-T signal of opportunity,” in *Radar Conference (Radar), 2014 International*, Oct 2014, pp. 1–4.
- [39] M. Conti, F. Berizzi, M. Martorella, E. Mese, D. Petri, and A. Capria, “High range resolution multichannel DVB-T passive radar,” *Aerospace and Electronic Systems Magazine, IEEE*, vol. 27, no. 10, pp. 37–42, Oct 2012.
- [40] H. Kuschel, M. Ummenhofer, D. O’Hagan, and J. Heckenbach, “On the resolution performance of passive radar using DVB-T illuminations,” in *Radar Symposium (IRS), 2010 11th International*, June 2010, pp. 1–4.
- [41] J. Gutierrez del Arroyo and J. , “WiMAX OFDM for passive SAR ground imaging,” *Aerospace and Electronic Systems, IEEE Transactions on*, vol. 49, no. 2, pp. 945–959, APRIL 2013.
- [42] M. Malanowski, K. Kulpa, M. Dryjaski, and S. Pietrzyk, “Fixed WiMAX (IEEE 802.16d) base station signal analysis for passive radar applications,” *Proc. SPIE*, vol. 7502, pp. 75 020V–75 020V–6, 2009. [Online]. Available: <http://dx.doi.org/10.1117/12.837900>
- [43] S. Wacks and B. Yazici, “Bistatic Doppler-SAR DPCA imaging of ground moving targets,” in *Radar Conference, 2014 IEEE*, May 2014, pp. 1071–1074.
- [44] L. Wang and B. Yazici, “Ground moving target imaging using ultra-narrowband continuous wave synthetic aperture radar,” *Geoscience and Remote Sensing, IEEE Transactions on*, vol. 51, no. 9, pp. 4893–4910, Sept 2013.
- [45] —, “Bistatic synthetic aperture radar imaging of moving targets using ultra-narrowband continuous waveforms,” *SIAM Journal on Imaging Sciences*, vol. 7, no. 2, pp. 824–866, 2014.
- [46] D. Donoho, “Compressed sensing,” *Information Theory, IEEE Transactions on*, vol. 52, no. 4, pp. 1289–1306, April 2006.
- [47] E. J. Candes, M. B. Wakin, and S. P. Boyd, “Enhancing sparsity by reweighted ℓ_1 minimization,” *Journal of Fourier analysis and applications*, vol. 14, no. 5-6, pp. 877–905, 2008.
- [48] B. Recht, M. Fazel, and P. Parrilo, “Guaranteed minimum-rank solutions of linear matrix equations via nuclear norm minimization,” *SIAM Review*, vol. 52, no. 3, pp. 471–501, 2010.
- [49] T. T. Cai and A. Zhang, “Sharp RIP bound for sparse signal and low-rank matrix recovery,” *Applied and Computational Harmonic Analysis*, vol. 35, no. 1, pp. 74–93, 2013.
- [50] E. Candes and T. Tao, “The power of convex relaxation: Near-optimal matrix completion,” *Information Theory, IEEE Transactions on*, vol. 56, no. 5, pp. 2053–2080, May 2010.
- [51] E. Candes and B. Recht, “Exact matrix completion via convex optimization,” *Foundations of Computational Mathematics*, vol. 9, no. 6, pp. 717–772, 2009. [Online]. Available: <http://dx.doi.org/10.1007/s10208-009-9045-5>
- [52] A. Chai, M. Moscoso, and G. Papanicolaou, “Array imaging using intensity-only measurements,” *Inverse Problems*, vol. 27, no. 1, p. 015005, 2011. [Online]. Available: <http://stacks.iop.org/0266-5611/27/i=1/a=015005>
- [53] E. Candes, Y. Eldar, T. Strohmer, and V. Voroninski, “Phase retrieval via matrix completion,” *SIAM Journal on Imaging Sciences*, vol. 6, no. 1, pp. 199–225, 2013.
- [54] Z. Weng and X. Wang, “Low-rank matrix completion for array signal processing,” in *Acoustics, Speech and Signal Processing (ICASSP), 2012 IEEE International Conference on*, March 2012, pp. 2697–2700.
- [55] L. Demanet and P. Hand, “Stable optimizationless recovery from phaseless linear measurements,” *Journal of Fourier Analysis and Applications*, vol. 20, no. 1, pp. 199–221, 2014. [Online]. Available: <http://dx.doi.org/10.1007/s00041-013-9305-2>
- [56] E. Candes and T. Strohmer, “Phaselift: Exact and stable recovery from magnitude measurements via convex programming,” *Comm Pure Appl Math*, vol. 66, pp. 1241–1274, 2013.
- [57] L. Demanet and V. Jugnon, “Convex recovery from interferometric measurements,” *CoRR*, vol. abs/1307.6864, 2013. [Online]. Available: <http://dblp.uni-trier.de/db/journals/corr/corr1307.html>
- [58] D. Yang, G. Liao, S. Zhu, X. Yang, and X. Zhang, “Sar imaging with undersampled data via matrix completion,” *Geoscience and Remote Sensing Letters, IEEE*, vol. 11, no. 9, pp. 1539–1543, Sept 2014.
- [59] M. Dao, L. Nguyen, and T. Tran, “Temporal rate up-conversion of synthetic aperture radar via low-rank matrix recovery,” in *Image Processing (ICIP), 2013 20th IEEE International Conference on*, Sept 2013, pp. 2358–2362.
- [60] Y. Nesterov, *Introductory Lectures on Convex Programming a Basic course*. Springer, 2004, vol. 1.
- [61] A. Beck and M. Teboulle, “A fast iterative shrinkage-thresholding algorithm for linear inverse problems,” *SIAM Journal on Imaging Sciences*, vol. 2, no. 1, pp. 183–202, 2009.
- [62] P. Combettes and J. Pesquet, “Proximal splitting methods in signal processing,” in *Fixed-Point Algorithms for Inverse Problems in Science and Engineering*, H. H. Bauschke, R. S. Burachik, P. L. Combettes, V. Elser, D. R. Luke, and H. Wolkowicz, Eds. New York: Springer, 2011.
- [63] C. Yarman, B. Yazici, and M. Cheney, “Bistatic synthetic aperture radar imaging for arbitrary flight trajectories,” *Image Processing, IEEE Transactions on*, vol. 17, no. 1, pp. 84–93, Jan 2008.
- [64] E. Candes, L. Demanet, and L. Ying, “Fast computation of fourier integral operators,” *SIAM Journal on Scientific Computing*, vol. 29, no. 6, pp. 2464–2493, 2007.
- [65] M. Fazel, H. Hindi, and S. Boyd, “A rank minimization heuristic with application to minimum order system approximation,” in *In Proceedings of the 2001 American Control Conference*, 2001, pp. 4734–4739.
- [66] M. Fazel, “Matrix rank minimization with applications,” Ph.D. dissertation, Stanford University, 2002.
- [67] T. Kariya and H. Kurata, *Generalized Least Squares*, 1st ed., ser. Wiley Series in Probability and Statistics. Wiley, 2004.
- [68] S. Wacks and B. Yazici, “Passive synthetic aperture hitchhiker imaging of ground moving targets part 2: Performance analysis,” *Image Processing, IEEE Transactions on*, vol. 23, no. 9, pp. 4126–4138, Sept 2014.
- [69] S. Xiao, J. D.C. Munson, S. Basu, and Y. Bresler, “An $N^2 \log N$ back-projection algorithm for SAR image formation,” in *Signals, Systems*

and Computers, 2000. Conference Record of the Thirty-Fourth Asilomar Conference on, vol. 1. IEEE, 2000, pp. 3–7.

- [70] V. Krishnan, J. Swoboda, C. Yarman, and B. Yazc, “Multistatic synthetic aperture radar image formation,” *Image Processing, IEEE Transactions on*, vol. 19, no. 5, pp. 1290–1306, May 2010.

APPENDIX

In this appendix, we derive an expression for C_{ij} under the zero-mean and statistical independence assumptions as outlined in Section III. Under these assumptions,

$$\begin{aligned} C_{ij}(\omega, s; \omega', s') &= [\mathcal{F}_i[\mathcal{R}](\omega, s; \omega', s')C_j(\omega, s; \omega', s') \\ &+ \mathcal{F}_j[\mathcal{R}](\omega, s; \omega', s')C_i(\omega, s; \omega', s') \\ &+ C_i(\omega, s; \omega', s')C_j(\omega, s; \omega', s')] \\ &\times \delta(\omega - \omega')\delta(s - s') \quad i, j = 1, 2 \quad i \neq j. \end{aligned} \quad (33)$$

and $C_{ij}(\omega, s; \omega', s') = 0$ for $(\omega, s) \neq (\omega', s')$. Now,

$$\begin{aligned} \mathcal{F}_i[\mathcal{R}](\omega, s; \omega, s) &= \int e^{i2\pi \frac{\omega}{c_0} r_{i,i}(s, \mathbf{x}, \mathbf{x}', \hat{\mathbf{y}})} A_i(\omega, s, \mathbf{x}, \mathbf{y}) \\ &\times A_i^*(\omega, s, \mathbf{x}', \mathbf{y}) \tilde{\rho}(\mathbf{x}) \tilde{\rho}^*(\mathbf{x}') d\mathbf{x} d\mathbf{x}' \end{aligned} \quad (34)$$

where

$$r_{ii}(s, \mathbf{x}, \mathbf{x}', \hat{\mathbf{y}}) = |\mathbf{x} - \gamma_i(s)| - |\mathbf{x}' - \gamma_i(s)| + \hat{\mathbf{y}} \cdot (\mathbf{x} - \mathbf{x}'). \quad (35)$$

We exploit the small-scene and far-field assumptions on $|\mathbf{x} - \gamma_i(s)|$ and $|\mathbf{x}' - \gamma_i(s)|$ to approximate r_{ii} as

$$r_{ii}(s, \mathbf{x}, \mathbf{x}', \hat{\mathbf{y}}) = (\hat{\gamma}_i(s) + \hat{\mathbf{y}}) \cdot (\mathbf{x} - \mathbf{x}'). \quad (36)$$

If we make the assumption that $A_i(\omega, s, \mathbf{x}, \mathbf{y}) \approx \lambda_i$, where λ_i is a constant, then using (36), (34) becomes

$$\mathcal{F}_i[\mathcal{R}](\omega, s; \omega, s) = |\lambda_i|^2 \int e^{i2\pi \frac{\omega}{c_0} (\hat{\gamma}_i(s) + \hat{\mathbf{y}}) \cdot (\mathbf{x} - \mathbf{x}')} \quad (37)$$

$$\tilde{\rho}(\mathbf{x}) \tilde{\rho}^*(\mathbf{x}') d\mathbf{x} d\mathbf{x}' \quad (38)$$

$$= |\lambda_i|^2 \int e^{i2\pi \frac{\omega}{c_0} (\hat{\gamma}_i(s) + \hat{\mathbf{y}}) \cdot \mathbf{x}} \tilde{\rho}(\mathbf{x}) d\mathbf{x} \quad (39)$$

$$\times \int e^{-i2\pi \frac{\omega}{c_0} (\hat{\gamma}_i(s) + \hat{\mathbf{y}}) \cdot \mathbf{x}'} \tilde{\rho}^*(\mathbf{x}') d\mathbf{x}' \quad (40)$$

$$= |\lambda_i|^2 \left| \int e^{i2\pi \frac{\omega}{c_0} (\hat{\gamma}_i(s) + \hat{\mathbf{y}}) \cdot \mathbf{x}} \tilde{\rho}(\mathbf{x}) d\mathbf{x} \right|^2 \quad (41)$$

$$= |\lambda_i|^2 \left| \hat{\tilde{\rho}}(\omega(\hat{\gamma}_i(s) + \hat{\mathbf{y}})) \right|^2. \quad (42)$$

The $\hat{\tilde{\rho}}$ denotes the Fourier transform of $\tilde{\rho}$.

Using (42),

$$\|f\|_{\mathcal{C}^{-1}}^2 = \int \alpha(\omega, s) |f(\omega, s)|^2 d\omega ds \quad (43)$$

$$\alpha(\omega, s) = \frac{1}{a(\omega, s) + b(\omega, s) + c(\omega, s)} \quad (44)$$

$$a(\omega, s) = |\lambda_i|^2 \sigma_j^2(\omega, s) \left| \hat{\tilde{\rho}}(\omega(\hat{\gamma}_i(s) + \hat{\mathbf{y}})) \right|^2 \quad (45)$$

$$b(\omega, s) = |\lambda_j|^2 \sigma_i^2(\omega, s) \left| \hat{\tilde{\rho}}(\omega(\hat{\gamma}_j(s) + \hat{\mathbf{y}})) \right|^2 \quad (46)$$

$$c(\omega, s) = \sigma_i^2(\omega, s) \sigma_j^2(\omega, s) \quad (47)$$

where $\sigma_i^2(\omega, s) = C_i(\omega, s; \omega, s)$ and $\sigma_j^2(\omega, s) = C_j(\omega, s; \omega, s)$. Thus, solving (24) requires prior knowledge of $\hat{\tilde{\rho}}$. If nothing

is known about $\hat{\tilde{\rho}}$, we make the assumption that $\hat{\tilde{\rho}}$ has a flat spectrum, say equal to 1. In other words, we weigh each Fourier component equally.

A. Optimization under i.i.d. stationary assumption and uninformative $\hat{\tilde{\rho}}$

Assume now that the noise at each receiver is i.i.d. stationary process, i.e. $C_i(\omega, s; \omega', s') = \sigma_i^2 \delta(\omega - \omega') \delta(s - s')$. In such a case, and under uninformative flat $\hat{\tilde{\rho}}$, (43) becomes

$$\|f\|_{\mathcal{C}^{-1}}^2 = \beta \|f\|_{\mathcal{L}^2}^2 \quad (48)$$

where

$$\beta = \frac{1}{\sigma_j^2 |\lambda_i|^2 + \sigma_i^2 |\lambda_j|^2 + \sigma_i^2 \sigma_j^2}. \quad (49)$$

Thus, in the objective functional (26), we can set $\mathbf{Q} = \mathbf{I}$ and rescale λ so that the new regularization parameter is $\tilde{\lambda} = \lambda/\beta$. This implies that under white noise and flat $\hat{\tilde{\rho}}$, the optimization procedure as described in Section III is the same as for noiseless case, with noise level only affecting the choice of λ .



Eric Mason Eric Mason received his B.Sc. in Electrical Engineering from Manhattan College in Bronx, NY, in 2012. He is currently pursuing a Ph.D. in Electrical Engineering at Rensselaer Polytechnic Institute in Troy, NY. His research interests are in passive radar imaging and applications of compressed sensing and low-rank matrix recovery in radar signal processing.



Il-Young Son Il-Young Son received his B.Sc. and M.Sc. degrees in Electrical and Electronics Engineering from Rensselaer Polytechnic Institute in Troy, NY. His M.Sc. thesis was on Diffuse Optical Tomography and Functional NIR imaging. He is currently a Ph.D. candidate in Electrical Engineering at Rensselaer Polytechnic Institute in Troy, New York. His research interest is in passive radar imaging, radar polarimetry, application of low-rank matrix and tensor recovery and compressive sensing techniques in radar.



Birsan Yazıcı Birsan Yazıcı received BS degrees in Electrical Engineering and Mathematics in 1988 from Bogazici University, Istanbul Turkey and MS and Ph.D. degrees in Mathematics and Electrical Engineering both from Purdue University, W. Lafayette IN, in 1990 and 1994, respectively. From September 1994 until 2000, she was a research engineer at General Electric Company Global Research Center, Schenectady NY. During her tenure in industry, she worked on radar, transportation, industrial and medical imaging systems. From 2001 to June 2003,

she was an assistant professor at Drexel University, Electrical and Computer Engineering Department. In Fall 2003, she joined Rensselaer Polytechnic Institute where she is currently a full professor in the Department of Electrical, Computer and Systems Engineering and in the Department of Biomedical Engineering.

Prof. Yazıcı's research interests span the areas of statistical signal processing, inverse problems in imaging, image reconstruction, biomedical optics, radar and X-ray imaging. She served as an associate editor for the IEEE Transactions on Image Processing from 2008 to 2012, and for SIAM Journal on Imaging Science from 2010-2014. She currently serves as an associate editor for IEEE Transactions on Geosciences and Remote Sensing. She is the recipient of the Rensselaer Polytechnic Institute 2007 and 2013 School of Engineering Research Excellence Awards. She holds 11 US patents.